Multi-scale interactions in an idealized Walker circulation: Mean circulation and intra-seasonal variability

Joanna Slawinska, * Olivier Pauluis, Andy Majda

Center for Atmosphere Ocean Science, Courant Institute of Mathematical Sciences, New York University, NY, NY

and Wojciech Grabowski

National Center for Atmospheric Research, Boulder, CO

* *Corresponding author address:* Joanna Slawinska, New York University, Courant Institute of Mathematical Sciences, Center for Atmosphere Ocean Science, 251 Mercer St., New York, NY 10012.

E-mail: joannaslawinska@nyu.edu

ABSTRACT

A high resolution cloud resolving model (CRM) simulation is developed here for a two-dimensional Walker circulation over a planetary scale domain of 40000 km for an extended period of several hundred days. The Walker cell emerges as the time averaged statistical steady state with a prescribed sinusoidal sea surface temperature (SST) pattern with mean temperature of 301.15 K and horizontal variation of 4 K. The circulation exhibits intra-seasonal variability on a time-scale of about 20 days with quasi-periodic intensification of the circulation and broadening of the convective regime. This variability is closely tied to synoptic scale systems associated with expansion and contraction of the Walker circulation. An index for the low frequency variability is developed using an Empirical Orthogonal Function (EOF) analysis and by regressing various dynamic fields on this index. The low frequency oscillation has four main stages: a suppressed stage with strengthened mid-level circulation, intensification phase, active phase with strong upper level circulation and a weakening phase. Various physical processes occurring at these stages are discussed as well as the impact of organized convective systems on the large scale flow.

1. Introduction

The dynamics of the tropical atmosphere is dominated by the complex interplay between convective motions and circulation on the large scales. Convection accounts for most of the vertical energy transport and usually involves horizontal scales of 100 km or less. Yet, convective activity is strongly modulated by atmospheric variability on the synoptic and planetary scales such as the Walker and Hadley circulations, the Madden Julian Oscillation, monsoons and equatorially-trapped waves (Lau and Waliser 2011). This interplay involves a wide range of processes, such as condensation and precipitation, radiative transfer and interactions with the ocean and land surfaces. As a result, an accurate representation of convective processes remains a central challenge in modeling the atmosphere and a major source of uncertainty in climate and weather prediction (Lin et al. 2006). A proper representation of the impacts of convective motions on the atmospheric flow at larger scales requires improvement in understanding the numerous multi-scale interactions that are involved (Mocrieff et al. 2007).

This paper investigates such interactions in the context of a highly idealized simulation of large-scale tropical circulation forced by variations in surface sea temperature (SST). The temperature difference between the warm Western Pacific and colder Eastern Pacific in the equatorial regions gives rise to a basin-wide flow known as the Walker Circulation, ascending over the warm pool and descending over the Eastern Pacific. This planetary-scale pattern is associated with strong variations of convective activity, with intense deep convection over the warm water, and much weaker shallow convection over the eastern part of the Pacific. Far from being steady, the Walker circulation exhibits variability on inter-annual, seasonal and intra-seasonal time scales. In particular, intra-seasonal variability associated with Madden Julian Oscillation (MJO, Madden and Julian 1972) has a strong signal over the Western Pacific, with a peak period of about 40-50 days.

While significant progress has been made over the last four decades, our understanding of driving mechanisms underlying the MJO remains unsatisfactory (Zhang 2005). Recent studies have emphasized the role of water vapor (Majda and Stechmann 2009, 2011; Raymond et al. 2009). In particular, large-scale advection of moisture has been suggested recently to play a role for the MJO. Modulation of convective activity occurs as a result of the interactions between large-scale flow and deep convection in which advection of water vapor plays a critical role. The critical role of moisture is supported by observational evidence which shows strong correlation between free tropospheric moisture and precipitation in the tropics (Bretherton et al. 2004). For example, Kiranmayi et. al. (2011) found that vertical buildup of moisture in front and subsequent horizontal advection of moisture play important role for MJO. Several studies have also found improvement in the way MJO is simulated if mid-tropospheric moisture is taken into account (see Lau and Waliser 2011, for more evidence). For example, Grabowski and Moncrieff (2004) show that the MJO weakens in a simulation where moisture-convective feedback is suppressed by artificial relaxation of mid-tropospheric moisture and cloudiness perturbation. Khouider and Majda (2006) and Khouider et al. (2010) have developed idealized multi-cloud models, where the representation of different types of tropical clouds and convective regimes depends crucially on the mid-tropospheric dryness. In these simplified models, dry mid-troposphere is first moistened by detrainment from low-level clouds that allows for a subsequent buildup of favorable conditions for deep convection. These models have been shown to improve the simulation of the wide range of tropical phenomena, from mesoscale and synoptic scale features (Frenkel et. al. 2012) to the MJO (Khouider et al. 2011).

In addition to the role of water vapor, several studies have emphasized the fact that interactions between different scales are crucial for the MJO. Majda and Biello (2004) argue that many observational features of the MJO (such as vertical structure in the westerly wind burst region or westerly midlevel inflow in the strong westerly flow region) are often poorly represented in large-scale atmospheric models, but can be successfully reconstructed in their multiscale model. In their analysis, the emergence of the MJO-like circulation depends on the upscale transfer of thermal energy and momentum from an eastward-propagating prescribed synoptic-scale circulation and heating. Other studies have also confirmed the significant impact of convective momentum transport (CMT) onto the large-scale flow by organized convective systems (Houze 2004; Moncrieff et al. 2007). Moreover, a theory for two-way feedback in the MJO has been developed by Khouider et al. (2012), based on an idealized two-way interaction dynamic model (Majda and Stechmann 2009). In this case, the large-scale MJO-like flow was modulated by CMT from synoptic scale systems. Due to modified large-scale conditions, vertical shear in particular, organized convective systems have been found to develop in preferred regions within the MJO with a preferred speed and direction of propagation. The prediction of this theory is in broad qualitative agreement with observations of the TOGA-COARE field campaign.

In this paper, we study an idealized planetary-scale circulation driven by large-scale variation in SST in a situation that can be viewed of as an analog for the Walker circulation. We rely on a high-resolution cloud resolving model and perform a detailed analysis of the simulated large-scale flow; we focus here on identifying low-frequency variability of the large-scale flow, and explaining how this frequency emerges from multi-scale interactions. In particular, we describe how convective variability depends on large-scale circulation. We show examples of convective organization and contrast them to illustrate how convective organization depends on evolving large-scale conditions. A secondary goal is also to establish a benchmark simulation that can be used as a reference point to evaluate the same circulation simulated with a less accurate model. In particular, our subsequent work will evaluate a Sparse Space and Time Super-Parameterization (SSTSP) approach (Xing et al. 2009) to represent the convective process based on its ability to accurately reproduce the interaction between convection and the planetary circulation discussed here.

The experimental set-up used here is closely related to the one originally presented in Grabowski et al. (2000). That paper considers the interactions between moist convection and the large-scale flow driven by a large-scale gradient of sea surface temperature and prescribed radiation. A cloud resolving model has been applied there to simulate 60 days of convective and large-scale dynamics resolved in the 2d domain with a horizontal extent of 4000 km. The mean circulation has been simulated quite successfully, with large-scale ascent and descent above the warm and cool parts of the surface. The simulated mean circulation is composed of first and second baroclinic modes, with distinct inflow to the center of the domain in the lower and middle troposphere and outflow in the higher parts of the troposphere. Convection is initiated periodically (about every two days) in the warmest part of the domain and then propagates towards colder areas. No detailed description of convective systems (their origin and structure, dependence on large-scale conditions) has been presented, besides noting the variety of simulated organization. Moreover, a two-day oscillation of the large-scale circulation has been found and its occurrence attributed to convectively initiated gravity waves that subsequently propagate across the domain and modify the large-scale flow. No detailed analysis the moisture response or how it modifies the oscillation of the large-scale flow has been given. However, this may be of little importance in the earlier case of Grabowski et al. (2000), since it is known that moisture responds to flow fluctuations on a much slower timescale. Our experimental set-up is based on a two-dimensional Walker cell set-up similar to Grabowski et al. (2000) but performed over a planetary scale domain of 40000 km and for an extended period of several hundreds of days, thus greatly expanding the spatial and temporal scales covered by the simulation.

The paper is organized as follows. The experimental setup is described in section 2. The results of our numerical simulations are discussed in section 3. It is shown that the large-scale SST gradient gives rise to a Walker Cell circulation. The circulation exhibits intra-seasonal variability on a time-scale of about 20 days with quasi-periodic intensification of the circulation and broadening of the convective regions. This variability is also closely tied to synoptic-scale systems associated with the expansion and contraction of the Walker circulation. Section 4 presents a systematic analysis of low frequency variability. An index for the low frequency variability is obtained using an Empirical Orthogonal Function (EOF) analysis and then applied to obtain a description of the oscillation by regressing the various dynamic fields on this index. The oscillation is decomposed into four main stages - suppressed phase, intensification, active phase and weakening - and various physical processes occurring at these stages are discussed. In Section 5 we focus on organized convective systems, in particular we contrast two different types of convective organization and their impact on the large-scale flow.

2. Model set-up

In this study, we use the EULAG model of Smolarkiewicz and Margolin (1997). The dynamical core is based on the anelastic approximation and uses finite-difference dynamics based on the MPDATA scheme (Smolarkiewicz 2006). This advection scheme is monotonic and intrinsically dissipative, and the model is used without any additional subgridscale diffusion. The Eulerian version of the model is applied to simulate a two-dimensional model, with 40000 km horizontal scales and 24 km in the vertical with a uniform resolution of 2 km in the horizontal direction and 500 meters in the vertical. Periodic boundary conditions are used in the horizontal direction and a gravity wave absorber is added in the uppermost 8 km of the domain.

The microphysical representation follows the one described in Grabowski (1998), and includes two classes of condensate: cloud water and precipitation. These two classes represent either cloud water and rain for temperatures above 268 K or cloud ice and snow below 253 K. For the temperature range in between these two thresholds, the two classes are assumed to be a mixture of both of cloud water/ice and rain/snow, respectively, with the relative amount given by linear dependence on temperature. Consistently, microphysical processes are considered for liquid and solid condensate in an analogous way, with the details of the formulas depending on the temperature. In particular, the condensation rate (and latent heating related to that) of a given kind of cloud condensate is determined by the condition of no supersaturation, with the saturated mixing ratio defined with respect to either water or ice, or a value in between the two, depending on the temperature. Other microphysical processes taken into account are autoconversion, accretion, evaporation and fallout of precipitation. More details can be found in Grabowski (1998).

The model is forced by a combination of a prescribed radiative cooling and surface energy fluxes. The radiative cooling $\dot{Q}_{SAM}$ and atmospheric temperature profile T_{ref} come from a three dimensional radiative-convective equilibrium simulation performed with the System for Atmospheric Modeling (Khairoutdinov and Randall 2003) applying the NCAR CAM3 interactive radiation scheme (Kiehl et al. 1998). The profiles are shown in Figure 1. The total cooling is prescribed as

$$\dot{Q} = \dot{Q}_{SAM} + \frac{T - T_{ref}}{\tau_{rad}}, \tag{1}$$

with the radiative time-scale τ_{rad} set to 20 days, and T being local temperature.

Surface sensible and latent heat fluxes are obtained from a bulk formula

$$F = C_d U(\phi_{sfc} - \phi_{z=0}), \tag{2}$$

where ϕ denotes either potential temperature, θ, or water vapor mixing ratio, q_v, at the first level of the model (z=0) and at the surface (sfc). Surface values of potential temperature and water vapor mixing ratio equal local SST and the saturated value of water vapor mixing ratio for the given SST, respectively. Surface wind, U, is calculated as follows:

$$U = max[2, (u_{z=0}^2 + u_*^2)^{0.5}], \tag{3}$$

with convective velocity timescale, u_*, estimated as:

$$u_* = gHC_d[(\theta_{srf} - \theta_{z=0})/\theta_{srf} + 0.61(q_{srf} - q_{z=0})]^{0.5}. \tag{4}$$

Drag coefficient, C_d and height of the boundary layer, H, are assumed 10^{-3} and 600 m, respectively. The SST distributions is a cosine function, with 303.15 K in the center and 299.15 K at the lateral boundaries of the domain. The model is also used without any surface friction, to keep the similarity between our experimental set-up and the one used by Grabowski et al. (2000) on a smaller domain. This experimental set-up is designed to drive a large-scale circulation that shares many similarities with the Walker circulation in the Tropics. The model is run over 320 days with a time step of 15 s, with our analysis focusing on the last 270 days.

3. Results

a. Mean Walker circulation

The warm surface temperature drives enhanced convection, which generates a dominant-scale overturning circulation. In addition, the simulated atmosphere exhibits significant variability on the planetary, synoptic and meso-scales. In this section, we first focus on the mean planetary scale circulation before analyzing its variability in the next section.

Figure 2 shows the time averaged horizontal velocity, perturbation of virtual temperature from its mean horizontal value, equivalent potential temperature, water vapor mixing ratio, relative humidity and cloud water mixing ratio. The large-scale circulation is characterized by low-level convergence over the warm SST, with a double maximum in convergence at the surface and at approximately 6 km. The maximum wind in the inflow is about 10 m s^{-1} at the surface, with a secondary maximum of 5 m s^{-1}. This is balanced by an upper tropospheric divergence, which peaks at about 13 km and a maximum horizontal velocity of 20 m s^{-1}. This circulation corresponds to ascent over warm water and subsidence over the colder SST, as clearly evidenced by the time-averaged streamfunction (not shown). The averaged vertical velocity over the warm regions peaks at 1.5 cm s^{-1} at a height of 8 km. Downward velocity in the subsidence regions is around 1 cm s^{-1} at the same level.

The averaged circulation thus combines a first baroclinic mode structure (Majda 2003), corresponding to the low-level inflow and upper level outflow, but also a significant contribution from a second baroclinic mode (Khouider and Majda, 2006), associated with the secondary inflow maximum of horizontal velocity in the middle troposphere. This two-mode structure is also reflected in the temperature distribution. Figure 2b shows the departure of the virtual potential temperature from its horizontal mean value. On average, the atmosphere is warmer over the warm SST and colder over the cold water, which is consistent with a dynamical forcing necessary to drive the overturning circulation. However, the virtual potential temperature anomalies in the middle tropospheric are consistently of the opposite sign from its mean vertical value. Such anomalies are necessary to drive the mid tropospheric jet. Overall, the virtual temperature perturbations are small, on the order of 2 K, which is broadly consistent with the scaling of Majda (2007).

The large-scale circulation has a strong impact on the moisture and equivalent potential temperature distributions. The subsidence regions are particularly dry, with relative humidity as low as 5%, except for a shallow boundary layer of thickness of approximately 1 km. Convection in the subsidence regions is limited mostly to shallow convection, with little to no precipitation. The equivalent potential temperature shows a pronounced minimum right above the boundary layer, with θ_e as low 320 K, while the equivalent potential temperature increases to 350 K right at the surface. The ascending region is characterized by active, but highly intermittent, deep convection, with typical vertical velocity on the order of 10 m s^{-1}. The ascending region is significantly more moist - particularly in the middle troposphere - than the subsidence regions. The equivalent potential temperature exhibits a mid-troposheric minimum, with $\theta_e \approx 345$ K, but it is less pronounced and located at higher levels than in the subsidence regions. One can also observe that the maximum value of the equivalent potential temperature is not located over the warmest SST, but rather in the inflow regions where stronger surface winds enhance the evaporation and convection is less active.

Figures 3a and 3b show the mean precipitable water content and the mean precipitation rate. As noted above, the subsidence regions are very dry, with only approximately one third of the precipitable water as the ascending regions. The precipitable water increases almost linearly toward the ascending region, where it is approximately constant. The regions of constant precipitable water content closely match the regions of high precipitation, which indicates that the simulated convection acts to maintain the precipitable water close to a critical threshold value (at least on the planetary scale and long time scale).

Figure 3c and 3d show the surface sensible and latent heat fluxes. While SST variations drive the atmospheric circulation through these fluxes, these fluxes themselves exhibit a distinctly different structure from the SST (which is a basin-wide cosine function). Indeed, the bulk formula for the surface fluxes (2) depends not only on the surface temperature but also on the surface wind speed and atmospheric condition. For instance, the surface latent heat fluxes present twin maxima at about 15000 km and 25000 km which are closely related to the maximum surface wind. Nevertheless, both the sensible and latent heat fluxes are larger over warm SST than cold SST. In contrast, the atmospheric cooling, shown in Figure 3e, is fairly uniform horizontally. While the atmospheric cooling balances the surface fluxes when averaged on the entire domain, its variations cannot balance the much larger variations of the surface fluxes. Instead, the atmospheric circulation acts to transport energy from the warm SST regions to the colder SST regions, as shown in Figure 3f, which shows the divergence of the atmospheric energy transport:

$$\frac{\partial}{\partial x}\int_0^\infty \rho u(C_pT + L_vq + gz)dz. \qquad (5)$$

Here, C_pT+L_vq+gZ is the moist static energy, with C_p the specific heat of dry air at constant pressure, L_v the latent heat of vaporization, and g the gravitational acceleration. The total atmospheric energy transport also includes the transport of kinetic energy which has been omitted from this calculation, but is in general significantly smaller than the transport of moist static energy. Thus, the mean circulation is a thermally direct circulation which acts to transport energy from warm to cold.

b. *Transients*

The time-averaged Walker circulation does not correspond to any instantaneous realization of the flow. Instead, a large number of transients operate over a wide range of spatial and temporal scales. Figure 4 shows the evolution of the surface horizontal velocity over the last 270 days of the simulations. The large-scale circulation exhibits a cyclic behavior, with periods of intense overturning and strong wind alternating with periods of weaker circulation and more quiescent atmosphere. The more intense periods are characterized by strong surface winds reaching 20 m s^{-1}. They are also associated with a significant expansion of the convergence regions and enhanced precipitation over the warm water. In contrast, during a weak phase, the surface flow is very weak, to the point of almost vanishing, and the zone of convergence is much more narrow. The time it takes for the flow to switch between these different phases varies on a case-by-case basis, but, on average, this cycle takes approximately 20 days, thus corresponding to an intraseasonal oscillations on the planetary scales.

This variability on the global scale is also tightly coupled to fluctuations at the synoptic and meso-scale. These are visible in Figure 4 as propagating structures in the low level wind. To illustrate this, we focus on two instances of propagating disturbances that are delimited by the black boxes in Figure 4, and shown in greater detail in Figure 5a and c. The first case can be viewed as a synoptic-scale (super) squall line (Moncrieff 1981, 1992; Houze 2004), characterized by a propagating low level jet that follows a region of enhance convergence. Figure 5b, showing the cloud top temperature, indicates that the structure is indeed associated with very intense convection, with cloud top temperature as low as 200K, and a very large region of upper level stratiform clouds. This structure remains coherent for several days, propagates over several thousands of kilometers and only decays once it encounters dryer air masses over the cold water. Similar structures are often found during the intensification of the planetary scale circulations. A second example of coherent structure is shown in Figure 5c. It also appears as a large propagating system in a region of low level convergence. A key difference with the previous case, as can be noted from Figure 5d showing the cloud top temperature, lies in that several smaller meso-scale systems are embedded within the synoptic structure. This second type of system propagates preferentially toward the warm SST, and is associated with a contraction of the precipitation regions. These systems occur in very different environmental conditions and exhibit very different characteristics. While we will analyze these systems and their interaction with the planetary scale flow in greater detail in a subsequent study, we want to highlight here the close connection between these various synoptic scale features and the evolution of the planetary scale circulation.

We also observe fluctuations at smaller scales. To quantify this high frequency variability, we analyze the spatio-temporal spectrum obtained from a Fast Fourier Transform applied to the precipitation field averaged over 48 km subdomains for the last 270 days of the simulations. The power spectrum, which is similar to the one introduced by Wheeler and Kiladis (1999), is shown in Figure 6. The spectrum shows that the precipitation exhibits a broad range of variability, with somewhat more power at the lower frequencies and wave numbers. The variability peaks around the line corresponding to a propagation speed of 7 m s^{-1}, which is somewhat lower than the propagation speed typical of convectively coupled gravity waves of 15m s^{-1} found by Wheeler and Kiladis but happens to be the propagation speed of the typical 'super' squall line from Figure 5. It is also symmetric in the positive and negative directions, which can be attributed to the two-dimensional nature of the simulation, the lack of Coriolis force, and the fact that the SST distribution is equally symmetric.

4. Low frequency variability

Here, we perform a systematic analysis of the low frequency variability in the simulations based on Empirical Orthogonal functions (EOFs) of the surface wind from the last 270 days of the simulation. The leading EOF accounts for 36.3% of the total variance and is shown in Figure 7a. This EOF corresponds to a strengthening of the low level flow, with enhanced convergence over the precipitating region. The EOF coefficient $e_1(t)$ is also shown in Figure 7b and indicates an oscillatory behavior with period of stronger low level convergence (positive value of e_1) alternating with weaker convergence (corresponding to negative value of e_1). While $e_1(t)$ is not periodic, its power spectrum peaks for a period of about 20 days, corresponding to the intra-seasonal frequency band. This low frequency is very robust and appears as the leading EOF within a wide range of dynamical variables.

In order to better assess the dynamics of this low frequency variability, we compute the lag regression of various variables with the EOF coefficient. For any given variable $f(x,t)$ we define a typical anomaly field $< f > (x,\tau)$ by computing a lag-regressed value

$$< f > (x,\tau) = \frac{1}{\sigma_1(T-|\tau|)} \int e_1(t) f(x,t+\tau)\, dt, \tag{6}$$

with the integral taken between day 30 and day $(240-\tau)$ for positive τ and between day $30+|\tau|$ and day 240 for negative value. The quantity σ_1 is the standard deviation of the EOF coefficient e_1. The lag regression is computed for a lag τ varying from -10 days to 9 days with a 6 hour increment. If one adds the mean value of the field $\overline{f}(x,t)$ to its lag-regressed value, one obtains the typical evolution of the variable f associated with a positive EOF anomaly of amplitude equal to the standard deviation σ_1.

Figure 8a shows the Hovmoller diagram for the reconstructed surface wind $\overline{u}+ < u >$. Ten days before the peak amplitude, the surface winds are much weaker than average, with a maximum inflow velocity of the order of 5 m s^{-1}. The wind speed gradually increases to reach a peak amplitude of 14 m s^{-1} and the convergence over the center of the domain is strongly enhanced. This is followed by a gradual decay of the Walker cell. This reconstruction is in good qualitative agreement with the individual cases (Figure 4) discussed earlier.

Figure 8b show the reconstruction for the precipitation rate. Precipitation lags slightly the maximum low level convergence, peaking for $\tau \approx 1$days. Interestingly, the precipitation reaches its maximum value not at the center of the domain, but rather on the edges of the convergence regions. There is also a marked asymmetry between the amplification stage ($-8\text{days} < \tau < -3\text{days}$) when precipitation is relatively weak but occurs over a relatively broad area, and the decay phase ($3\text{days} < \tau < 8\text{days}$) when the precipitation weakens overall and is confined to a much narrower region. This asymmetry is also apparent in the reconstruction for the precipitable water shown in Figure 8c. There is a significant build up of water vapor in the amplification phase that occurs over a broad portion of the domain. In contrast, the decaying stage is still characterized by high water content in the central region, but there has been a substantial shrinking of the area with high water concentration.

In order to characterize the low frequency oscillation, we decompose the cycle into 4 phases, namely the suppressed phase corresponding to $\tau \leq -8$days and $\tau \geq 7$days, amplifying phase for $\tau \geq -8$days and $\tau \leq -3$days, peak phase for $\tau \geq -3$days and $\tau \leq 3$days and decaying phase that follows during $\tau \geq 3$days and $\tau \leq 8$days. We then compute the anomalies of horizontal wind, virtual temperature, equivalent potential temperature and cloud water mixing ratio in the middle of each phase. These are shown in Figures 9 - 12.

i. Suppressed phase

Figure 9 shows the anomalies associated with the suppressed phase at $\tau = -10$days. The overall structure of the anomaly corresponds to a weakening of the overturning flow. The horizontal velocity in the inflow is reduced by up to 4 m s^{-1} at the surface and by up to 6 m s^{-1} in the upper troposphere. A comparison with the structure of the mean flow (Figure 2) indicates however that the circulation anomaly is not simply promotional to the mean overturning. Instead, it exhibits a pronounced strengthening of the mid tropospheric jet at about $z = 6$ km by as much as 2 m s^{-1}. This intensification of the jet is associated with an increased advection of mid tropospheric dry air with low equivalent potential temperature into the central part of the domain that acts to suppress convection.

The virtual potential temperature anomaly indicates that the atmosphere as a whole is slightly colder than average. It also exhibits a quadrupole pattern: the lower troposphere is colder over the cold water, but the upper troposphere there is warmer. In effect, while the lower troposphere anomaly reflects the sea surface temperature distribution, the upper troposphere does not. This temperature anomaly results in an acceleration of the flow toward the warm water both in the lower and upper troposphere, and toward the colder regions in the middle troposphere.

In the upper troposphere, the equivalent potential temperature anomaly is almost identical to the virtual potential temperature anomaly but differs significantly below 6 km due to the variations of latent heat content of the air parcels. Overall, the θ_e anomaly is much more homogenous in the vertical, indicating that convective processes do a reasonable job at transmitting the θ_e anomaly from the surface through the entire air column. The most noticeable features here are the dry mid troposphere over the regions of active precipitation, which is likely tied to the stronger mid tropospheric jet, and the moist anomaly located over the coldest water that is a direct result of the weaker subsidence. These are also reflected in the condensed water anomalies, which show much reduced cloudiness associated with weaker convection over the central part of the domain, and a small positive anomaly over the cold SST.

ii. Strengthening phase

The low level flow intensifies from days -10 to days -5. The corresponding anomalies are shown in Figure 10. The surface anomaly is very weak, meaning that the surface winds are now close to the climatological average. In the mid-troposphere, the anomaly has reversed sign from $\tau = -10$days corresponding to a weaker than average mid-tropospheric jet. In the upper troposphere the circulation is sill weaker than average, though there is an indication of enhance divergence at the very center. The evolution from $\tau = -10$days to $\tau = -5$days is consistent with the virtual temperature anomaly discussed above with the early intensification of the circulation being primarily limited to the lower to mid troposphere.

The virtual temperature anomalies show a significant domain-wide cooling when compared to the situation at $\tau = -10$days, a direct results of the overall weak precipitation - and latent heat heating. The central regions are also now systematically warmer than the subsidence regions, which should lead to an intensification of a tropospheric deep overturning circulation. A large positive anomaly for the equivalent potential temperature of about $2K$ is present in the subsidence regions, indicative of a significant moistening. In the absence of deep convection there, it remains confined below 5 km. The cloud water anomaly also shows enhanced cloudiness over the subsidence regions. It also indicates that the region of deep convection is more narrow than usual, with a positive anomaly at the center surrounded by two negative anomalies.

iii. Active phase

Figure 11 shows the anomalies associated with the active phase at $\tau = 0$days corresponding to the strongest surface wind. The anomalies at $\tau = 0$days are almost the opposite to that at $\tau = -10$days which is consistent with the quasi-periodic behavior of the oscillation on a 20 days time-scale. The large-scale circulation has intensified dramatically and corresponds now to a tropospheric-deep overturning circulation. The atmosphere as a whole has warmed since $\tau = -5$days. The temperature anomaly exhibits a quadrupole structure that is similar but of opposite sign to the one observed at $\tau = -10$days. As argued above, this temperature would act to reinforce slightly the upper tropospheric circulation, but weakens the low level overturning.

The central region is now warmer and moister than average. The magnitude of the θ_e anomaly in the central region is about 2.5K which is comparable to the θ_e anomaly that is observed over the subsidence regions at $\tau = -5$days. A positive θ_e anomaly that developed over the subsidence regions during the inactive and amplifying phase was confined to the vertical region a few kilometers above the boundary layer. It spreads to the entire column once it reaches the regions of active convection during the active phase where it contributes to the overall warming of the atmosphere. Interestingly, the strongest convection occurs on the edge of the precipitation regions - as can be noted from both the θ_e anomaly and the cloud water anomaly - corresponding thus to a broadening of the region of active convection resulting from the inflow of moister air. This evolution of the θ_e anomaly here is a strong indication that horizontal advection of θ_e and moisture is a key ingredient to explain the intraseasonal modulation of the convective activity in our simulations.

iv. Decaying phase

Figure 12 shows the anomalies associated with the decaying phase at $\tau = 5$days. These anomalies are to a large extent opposite to the ones occurring during the strengthening phase at $\tau = -5$days. In particular, the anomalies over the central region correspond to a stronger than average mid-tropospheric inflow and upper tropospheric outflow. At the same time, surface anomalies of horizontal wind indicate a reduction of low-level inflow into the regions of active convection. Together, these anomalies indicate a reduction of the moisture and moist static energy transport into the convective regions, thus implying a further weakening and overall cooling trend.

The decaying phase also corresponds to the warmest mean atmospheric temperature, as a direct results of the extended period of enhanced convection. The mean atmospheric temperature increases by 2 K from $\tau = -5$days to $\tau = 5$days due to the enhanced precipitation. While the atmosphere is warmer overall, it is also dryer, most notably over the subsidence regions. The negative anomalies of θ_e in the boundary layer are comparable to the positive anomalies in the free troposphere, which indicates the internal energy increase associated with the warming in large part is compensated by a reduction of latent heat content. The low frequency oscillation thus corresponds to a switch back and forth between a regime with low sensible heat content but high latent heat corresponding to the amplifying phase and a regime with high sensible heat but low latent heat content during the decaying phase.

5. Organized convective systems

The low frequency variability of the Walker circulation discussed above is strongly coupled to changes in the organization of convection. We analyze here two separate systems, shown in Figure 5. The first system occurs during the expansion of the Walker circulation, while the second occurs during the contraction. As such they evolve in a very different large-scale environment, and their overall impact on the circulation (Moncrieff 1981, 1992) is also markedly different. While we focus here on two specific events, similar cases of convective organization are regularly found to be associated with the expansion and contraction of the Walker Cell cycle over 270 days of simulated period. Overall, the dependence of convective evolution on the low-frequency phase seems to be very robust.

The first system is shown in Panels a and b of Figure 5. It occurs between day 120 and day 127 during the strengthening phase of the low frequency variability, when the region of large-scale ascent is expanding. The system propagates into the subsidence region with an almost constant speed of about 6.7 m s^{-1}. It lasts for about 8 days, and dissipates after reaching colder ocean and drier atmosphere, having travelled for over 5000 km. In effect, the propagation of this system corresponds to the expansion of the convergence region, and similarly, its decay around day 127 coincides with the termination of this expansion. The surface wind, shown in Figure 5a, shows a strong low-level convergence of the flow, changing from a strong easterly ahead of the system to strong westerly behind it in a few hundred kilometers and in less than a day. As the system propagates, the large scale flow strengthens significantly during the first five days, with low level inflow reaching up to 20 m s^{-1}. This system occurs in a region of strong vertical shear.

Figure 13a shows the mean streamfunction associated with the first system. To obtain the figure, we average the horizontal velocity in the reference framework moving along the storm. The streamfunction is then obtained by computing the vertical integral of the mass transport. The system exhibits a very coherent structure, which is reminiscent of a squall line, although on a much broader horizontal scale. The streamfunction shows that the inflow is made of low level air coming from the subsidence region to the east. Two-thirds of the outflow (relative to the moving storm) is taking place behind the storm, while about one third is sent back in the upper troposphere ahead of the storm. Most of the mean ascent occurs within a narrow region of about 200 km.

Figure 13b shows the moving average of the equivalent potential temperature. The isentropes and streamlines are not parallel but instead exhibit significant crossing. This indicates that the mean streamlines are not representative of the parcels trajectories and that flow is highly intermittent. The inflow structure corresponds to a shallow moist boundary layer with high value of θ_e and a much dryer free troposphere. The low level outflow behind the storm has significantly lower value of θ_e than the inflow at the same level: the boundary layer air mass ahead of the storm has been almost entirely depleted and has been replaced by low θ_e air from the lower troposphere. The upper tropospheric outflow has a much larger value of θ_e and is made primarily of boundary layer air that have risen within the narrow ascent regions. One can also notice that the outflow ahead of the storm is significantly warmer than the outflow behind it. There is a sharp temperature gradient in the regions of mean ascent. Such a temperature gradient is necessary from a dynamical point of view to reverse the wind direction of the first baroclinic mode.

Shallow convection prevails in front of the system, as lower troposphere is moist due to strong surface winds and large surface fluxes. However, deep convection is severely inhibited due to the very dry middle troposphere. Shallow convection gradually moistens the lower troposphere as noticeable through the increase θ_e at about z=3.5 km ahead of the storm. Closer to the storm, at about x = 800 km in Figure 13b, the meso-scale flow exhibits weak ascent, which further reinforce the moistening of the lower troposphere. At the center of the storm, between x=200 km and x=400 km, deep convection occurs frequently there, and the corresponding strong updrafts are clearly marked by streamlines being almost vertical. Finally, the inflow of low θ_e air in the middle troposphere is gradually moving down through re-evaporation of stratiform precipitation and convective downdraft. This system exhibits a highly coherent structure typical for a squall line (Houze 2004) where the dynamics exhibits multiple forms of interaction with convection. Our analysis fits well with the three-cloud-type paradigm of Khouider and Majda (2006) with shallow cumulus clouds in the front part of the system, deep convection associated with the main ascent region, and extensive stratiform regions both ahead and behind the storm from Figure 13a. There is a strong jump updraft flow associated with the mean vertical shear in the super convective system (Liu and Moncrieff 2001). More will be said about the momentum budget of this system at the end of this section.

This system dissipates around day 128, after moving over colder water. The mid-troposphere at the time of the dissipation is anomalously dry due to strengthened advection of dry air by a well developed mid-tropospheric jet associated with the decaying stage of the low frequency oscillation. As soon as the system decays, the ascent region begins to collapse, a new organized structure forms at about 1500 km behind the first system (see Figure 5) and starts propagating toward the warm water at a speed of about 5.7 m s^{-1}. This is the second system we will analyze. This second system is associated with the weakening of the Walker circulation and a significant narrowing of the ascent region. In contrast to the first system, this second system is much less coherent, and corresponds rather to a westward propagating envelope of several individual convective systems that themselves propagate eastward.

The moving average of streamfunction and equivalent potential temperature for this second system are shown in Figure 13c and d. In effect, the second system propagates within the region that has been modified by the first system. Its large scale environment is thus characterized by a much weaker shear, moister lower troposphere but dryer boundary layer, and much weaker horizontal gradients. As for the first system, the streamlines and isentropes are not parallel, especially in the ascent regions, which indicates that parcel trajectories differ significantly from the mean streamlines due to convection and turbulence. The streamfunction is mostly barotropic (which is in part a result of using the horizontal velocity relative to the storm, with a broad regions of weak ascent between x=100 km and x=800 km). At the back of the storm, there is a marked low level inflow from the dry regions associated with a meso-scale downdraft. Evidence for this jet and mesoscale downdraft can also be inferred from the dipping of the low θ_e isentropes between x= 600 km and x = 100 km. This advection of dry air at the back of the storm acts to shut down convection behind the storm and creates the overall contraction of the precipitation region.

To diagnose the contribution of the various scales, here we analyze the momentum and θ_e transports between the synoptic, meso and convective scales. The upscale transport from the vertical flux of a variable f can be decomposed as

$$[\overline{wf}] = [\overline{w}][\overline{f}] + [(\overline{w^*})(\overline{f^*})] + [w'f'], \tag{7}$$

where the overline $\bar{\cdot}$ indicates a time average in the moving frame, the bracket $[\cdot]$ the horizontal average (limited to the moving domain shown in Figure 13), the asterisk $f* = \overline{f} - [\overline{f}]$ is the contribution for the stationary meso-scale structure and the prime $f' = f - \overline{f}$ corresponds to the transient fluctuations (Majda 2007). The first term equals the vertical flux by mean ascent. The second term corresponds to the transport by the time-mean mesoscale flow, whereas the third term account for the transport by transient fluctuations, primarily at the convective scale. The resulting fluxes of momentum and equivalent potential temperature are shown for system 1 and 2 in Figure 14 and 15, respectively.

The coherent structure of the first system is reflected in the spatial distribution of the fluxes. Convective and mesoscale fluxes are strongly localized, being particularly large in the central part of the system, where deep convection prevails. Mesoscale fluxes are stronger in the upper troposphere, where stratiform clouds spread. Convective fluxes are particularly large in the lower troposphere of the region with strong convective updrafts. Both convective and mesoscale fluxes are of comparable magnitude to the transport by mean ascent. Thus, their impact on the large-scale flow is not negligible. In particular, the convective flux of momentum strengthens the surface wind. Also it tends to weaken the mid-tropospheric jet and strengthen the upper-tropospheric outflow. The mesoscale momentum flux also enhances the upper tropospheric outflow. Both mesoscale and convective fluxes of equivalent potential temperature are responsible for a net upward transport of energy into the upper troposphere.

The second system does not reveal such coherency as the first one, which can be viewed as a result of the smaller embedded systems that propagate in the opposite direction to the main envelope (Majda and Stechmann 2009). The time-averaged convective and mesoscale fluxes are much less localized and weaken towards the direction where the embedded systems propagate. Still, convective and mesoscale fluxes have a significant impact onto the large-scales. In particular, the convective flux of momentum enhances low level inflow, although less intensively than in the first system, and contributes to the acceleration of the upper tropospheric outflow. Convective transport of equivalent potential temperature is significant, whereas the mesoscale flux is negligible. In summary, both systems impact large-scale flow and environmental conditions. In particular, convective fluxes of momentum act to accelerate low-level inflow and upper tropospheric outflow. Also, both systems tend to transport moist static energy upward efficiently. Since the first system is much more coherent than the second system, its overall impact is larger (Majda and Stechmann 2009).

6. Summary

In this paper, we analyze an idealized Walker circulation induced by large-scale gradient of sea surface temperature in a cloud resolving model. The time-mean circulation exhibits a planetary scale overturning, with enhanced deep convection over warm water, and suppressed convection over the subsidence regions. This Walker circulation, far from being steady, exhibits significant low frequency variability on a time scale of about 20 days characterized by an alternate between periods of intense circulation and precipitation and periods of weaker flow and convective activity.

A systematic statistical analysis of the low frequency variability has been presented. We use an EOF analysis of the surface winds to derive a low frequency index. We then compute the lag regression of various physical fields with this index. This approach makes it possible to identify the key physical processes associated with the low frequency variability. A typical cycle can be decomposed into four phase, a suppressed phase, strengthening phase; active phase, and decaying phase, with each phase lasting for 4-5 days. The suppressed phase is characterized by a weak circulation, weak convection and overall dry atmosphere. The intensification phase shows a significant increase in the water vapor content in the subsidence regions as well as a weakening of the mid-tropospheric jet found usually at about 3-4 km above the ground. The active phase occurs when the moisture anomaly generated in the subsidence regions has been advected into the region of active convection over the warm SST. This is followed by a marked warming and drying of the atmosphere, particularly pronounced over the subsidence regions, during the decaying phases.

From a dynamical point of view, the low frequency anomaly exhibits several characteristics of a fluctuation driven by moisture perturbations. In particular, the active phase is proceeded by gradual build up of water content of the atmosphere. As this build-up occurs primarily over the subsidence region, advection of moisture from the subsidence regions to the regions of active precipitation plays an important role in the onset of the active phase. Finally, the mid-tropospheric jet exhibits a very different phase from the overall overturning circulation. Indeed, we observe that the mid tropospheric jet is at its weakest during the intensification phase of the oscillation. As this mid-tropospheric jet brings dry, low entropy air into the precipitation regions, such shutdown of the low tropospheric jet leads to an increase in both water vapor and energy content of the main precipitating regions during the strengthening phase.

The active period also corresponds to an horizontal expansion of the deep convection into the otherwise dry regions, while the suppressed periods are usually associated with a significantly smaller precipitation area. An intriguing feature of this expansion and contraction of the precipitation regions lies in the fact that they are closely tied to synoptic-scale squall-like systems. Our analysis furthermore indicates that systems associated with the expansion of the precipitation zone differ significantly from those associated with the contraction. In other words, different phases of low-frequency variability tend to favour different forms of convective organization. These systems have, in turn, different feedback to the large-scales. This indicates a strong link between the low frequency variability and the behavior of synoptic scales.

The simulations here with a strong sinusoidal imposed SST pattern have super convective squall lines in the fluctuations but no large scale convectively coupled gravity waves. On the other hand, large domain two-dimensional simulations with constant SST are dominated by the mergence of synoptic scale convectively coupled Kelvin wave trains (Grabowski and Moncrieff 2001). The structure and strength of the imposed SST which leads to a mixture of mesoscale convective systems and convectively coupled gravity waves is an interesting issue which merits further investigation. This is beyond the computational resources available in the present study but could be studied through the stochastic multi-cloud model (Frenkel et al. 2012).

Acknowledgments.

J. Slawinska is supported as a postdoctoral fellow by CMG grant, DMS-1025468 while both O.P. and A.M. acknowledge funding from the Center for Prototype Climate Modeling at NYU Abu Dhabi.

Bretherton, C. S., M. E. Peters, and L. E. Back, 2004: Relationships between water vapor path and precipitation over the tropical oceans. J. Climate, 17, 1517-1528.

Frenkel, Y., Majda A.J., and B. Khouider, 2012: Using the stochastic multicloud model to improve tropical convective parameterization: A paradigm example. J. Atmos. Sci., 69:1080-1105.

Grabowski, W. W., 1998: Toward Cloud Resolving Modeling of Large-Scale Tropical Circulations: A Simple Cloud Microphysics Parameterization. J. Atmos. Sci., 55, 3283-3298.

Grabowski, W. W., Yano J.-I., and . W. Moncrieff, 2000: Cloud Resolving Modeling of Tropical Circulations Driven by Large-Scale SST Gradients. J. Atmos. Sci., 57, 2022-2040.

Grabowski, W. W., and M. Moncrieff, 2001: Large-scale organization of tropical convection in two-dimensional explicit simulations. Q. J. R. Meteorol. Soc., 127, 445-468.

Grabowski, W. W., and M. W. Moncrieff, 2004: Moisture-convection feedback in the tropics. Q. J. R. Meteorol. Soc. 130, 3081-3104.

Houze, R. A. Jr., 2004: Mesoscale convective systems. Rev. Geophys., 42:G4003+

Khairoutdinov, M. F., and D.A. Randall, 2003: Cloud-resolving modeling of the ARM summer 1997 IOP: Model formulation, results, uncertainties and sensitivities. J. Atmos. Sci., 60, 607-625.

Khouider, B. and A. J. Majda, 2006: A Simple Multicloud Parameterization for Convectively Coupled Tropical Waves. Part I: Linear Analysis. J. Atmos. Sci., 63, 1308-1323.

Khouider B., Biello J., and A. J. Majda, 2010: A stochastic multicloud model for tropical convection. Comm. Math. Sci., 8(1):187-216.

Khouider, B., St-Cyr A., Majda A. J., and J. Tribbia, 2011: The MJO and convectively coupled waves in a coarse-resolution GCM with a simple multicloud parameterization. J. Atmos. Sci., 68, 240-264.

Khouider, B., Ying H., Majda A. J., and S. N. Stechmann, 2012: Multiscale Waves in an MJO Background and Convective Momentum Transport Feedback. J. Atmos. Sci., 69, 915-933.

Kiehl J. T., Hack J. J., Bonan G. B., Boville B. A., Williamson D. L., and P. J. Rasch, 1998: The National Center for Atmospheric Research Community Climate Model: CCM3. J. Climate, 11, 11311149.

Kiranmayi, L. and E. D. Maloney, 2011: Intraseasonal moist static energy budget in reanalysis data, J. Geophys. Res., 116, D21117, doi:10.1029/2011JD016031.

Lau, W. K. and D. E. Waliser, 2011, Intraseasonal Variability in the Atmosphere-Ocean Climate System, Spinger-Praxis second edition.

Lin J-L., Kiladis G. N., Mapes B. E., Weickmann K. M., Sperber K. R., Lin M., Wheeler M. C., Schubert S. D., Del Genio A., Donner L. J. , Emori S., Gueremy J. F., Hourdin F., Rasch P. J., Roeckner E., and J. F. Scinocca, 2006: Tropical intraseasonal variability in 14 IPCC AR4 climate models. Part I: Convective signals. Journal of Climate, 19(12):26652690.

Liu, C. and M. Moncrieff, 2001: Cumulus ensembles in shear: implications for parameterizations J. Atmos. Sci., 58 (18), 2832-2842.

Madden, R., and P. Julian, 1971: Detection of a 40-50 day oscillation in the zonal wind in the tropical pacific. J. Atmos. Sci., 28:702708.

Majda A. J. and R. Klein, 2003: Systematic multiscale models for the Tropics. J. Atmos. Sci., 60, 393-408.

Majda, A. J., 2003: Introduction to PDEs and Waves for the Atmosphere and Ocean, volume 9 of Courant Lecture Notes in Mathematics. American Mathematical Society, Providence.

Majda, A. J. , and J. A. Biello, 2004: A multiscale model for the intraseasonal oscillation. Proc. Natl. Acad. Sci., 10, 4736-4741.

Majda. A. J., 2007: New multi-scale models and self-similarity in tropical convection. J. Atmos.Sci., 64, 1393-1404.

Majda, A. J. , and S. Stechmann, 2009: The Skeleton of Tropical Intraseasonal Oscillations, Proc. Nat. Acad.Sci., 106, 8417-8422.

Majda, A. J., and S. Stechmann, 2011: Nonlinerar dynamics and regional variation in the MJO Skeleton. J. Atmos. Sci., 68, 3053-3071.

Moncrieff M. W., 1981: A theory of organized steady convection and its transport properties. Quart. J. Roy. Meteor. Soc., 107:29-50.

Moncrieff M. W., 1992: Organized convective systems: Archetypical dynamical models, mass and momentum flux theory, and parameterization. Quart. J. Roy. Meteor. Soc., 118:819850.

Moncrieff M. W., Shapiro M., Slingo J., and F. Molteni, 2007: Collaborative research at the intersection of weather and climate. WMO Bulletin, 56:204211

Raymond, D. J., and F. Fuchs, 2009: Moisture Modes and the Madden-Julian Oscillation. J. Climate, 22, 3031-3046.

Smolarkiewicz, P. K., and L. G. Margolin, 1997: On forward-in-time differencing for fluids: An Eulerian/semi-Lagrangian nonhydrostatic model for stratified flows. Atmos.-Ocean, 35, 127-152.

Smolarkiewicz, P. K., 2006: Multidimensional positive definite advection transport algorithm: an overview. Int. J. Numer. Meth. Fluids, 50, 1123-1144. doi: 10.1002/fld.1071.

Wheeler, M., and G.N. Kiladis, 1999: Convectively coupled equatorial waves: Analysis of clouds and temperature in the wavenumber-frequency domain. J. Atmos. Sci., 56, 374-399.

Xing, Y., A. J. Majda, and W. W. Grabowski, 2009: New efficient sparse space-time algorithms for superparameterization on mesoscales. Mon. Wea. Rev., 137, 4307-4324.

Zhang, C., 2005: Madden-Julian Oscillation, Rev. Geophys., 43, RG2003, doi:10.1029/2004RG000158.

List of Figures

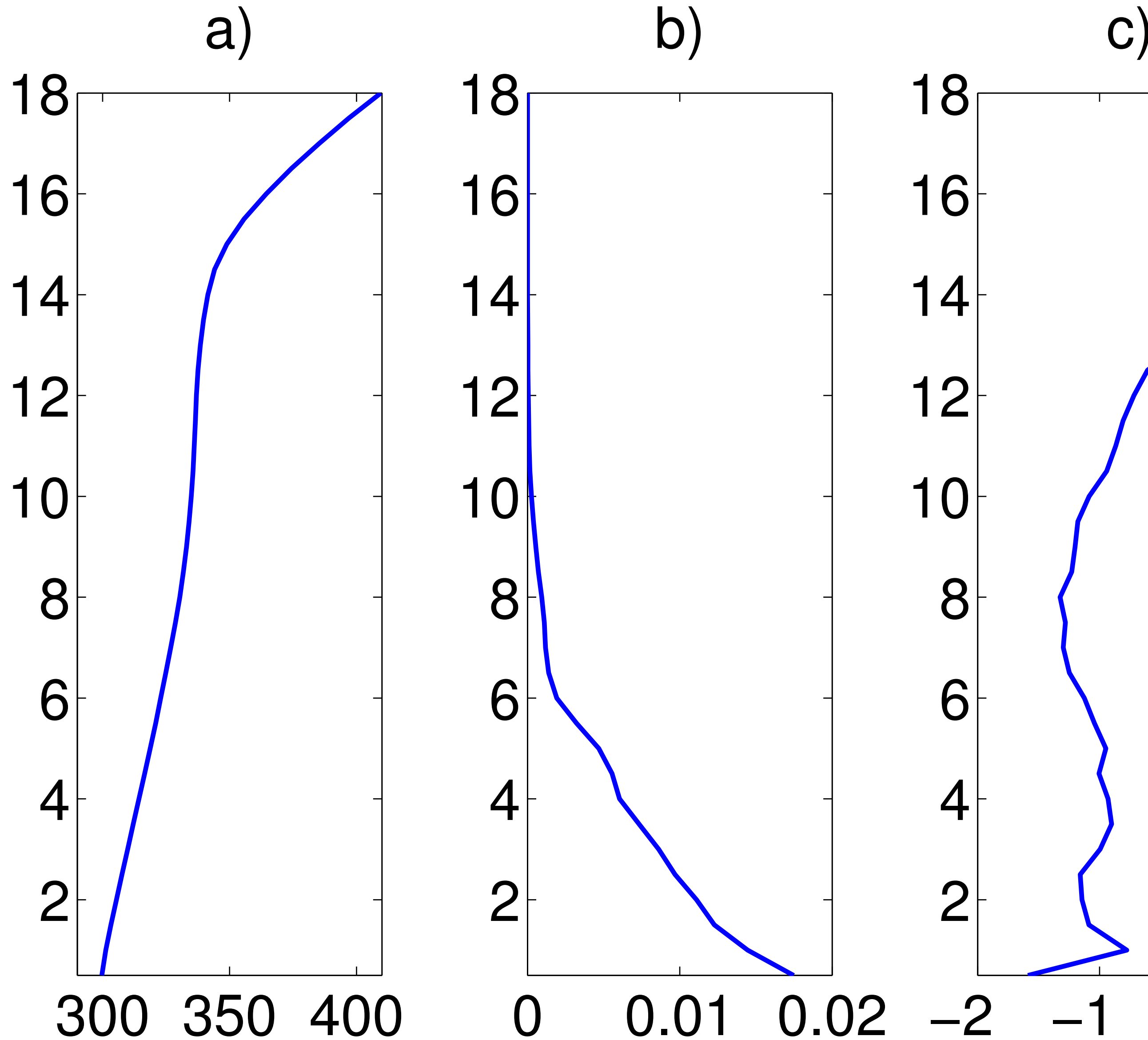

FIG. 1. Profile of a) environmental potential temperature (K); b) environmental water vapor mixing ratio (kg kg^{-1}); c) radiative cooling (K day^{-1}). Y axis: height (km).

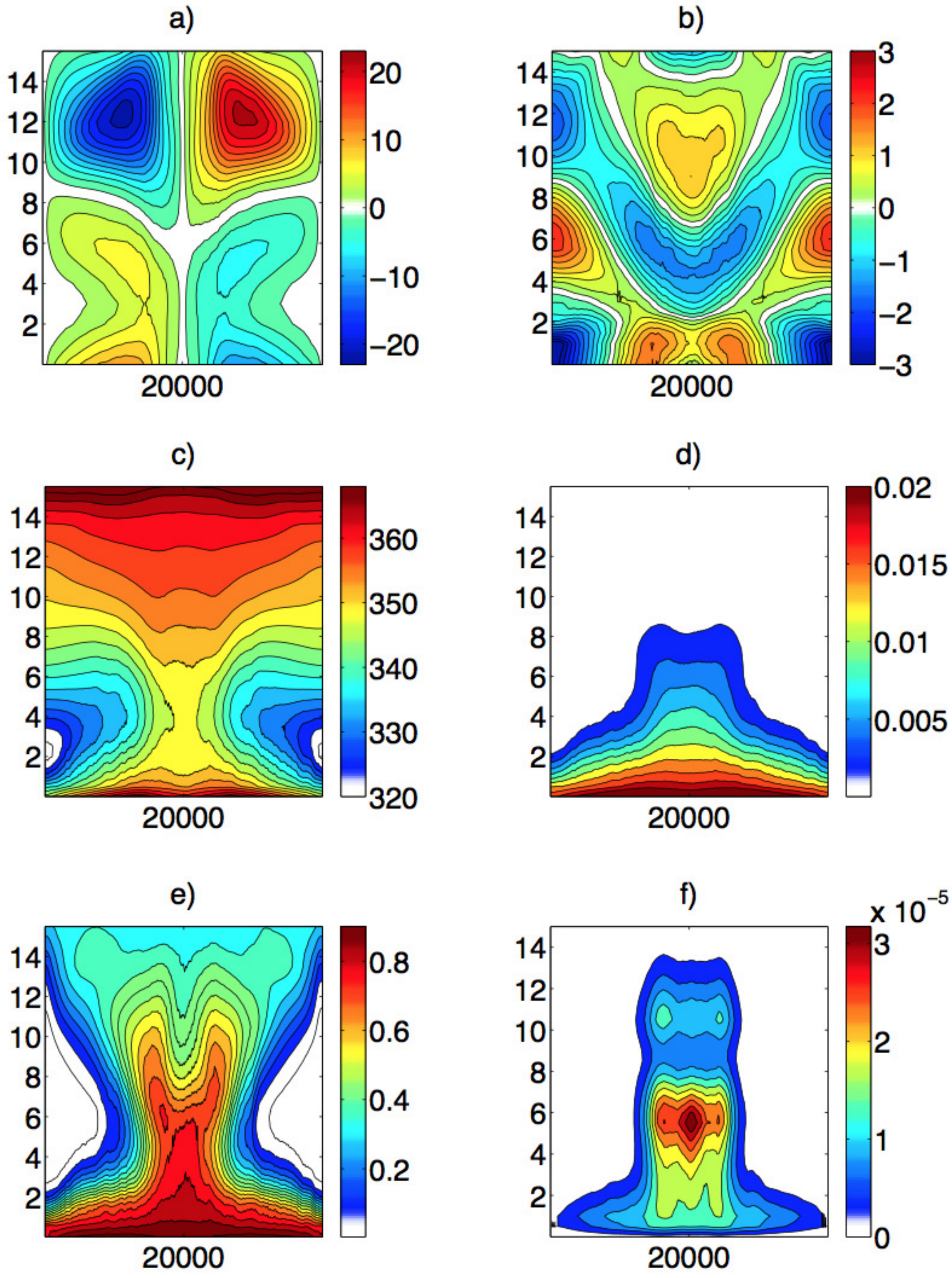

FIG. 2. Mean (in time) field of a) horizontal velocity (m s^{-1}), b) perturbation of virtual temperature from mean horizontal value (K), c) equivalent potential temperature (K), d) water vapor mixing ratio (kg kg^{-1}), e) relative humidity (%), and f) cloud water mixing ratio (kg kg^{-1}). Y axis: height (km).

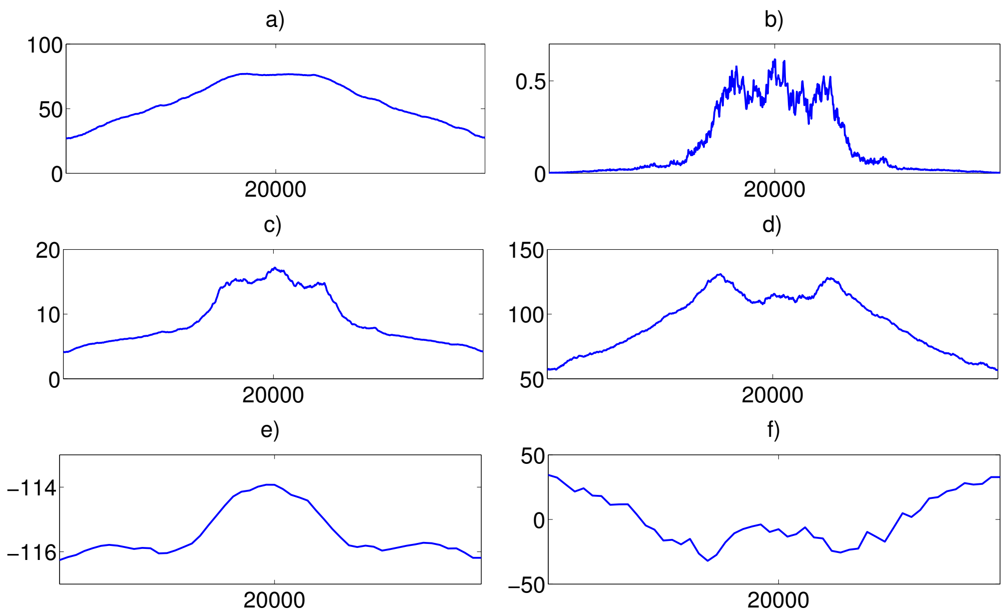

FIG. 3. Mean (in time) horizontal profiles of a) precipitable water content (kg m^{-2}), b) precipitation (mm h^{-1}), c) sensible surface flux (W m^{-2}), d) latent surface flux (W m^{-2}), e) vertical integral of radiative cooling (W m^{-2}), and f) divergence of integral of moist static energy in the column (W m^{-2}. All mean have been obtained by averaging over every time step of the last 273 days of the simulation). X axis: x direction (km).

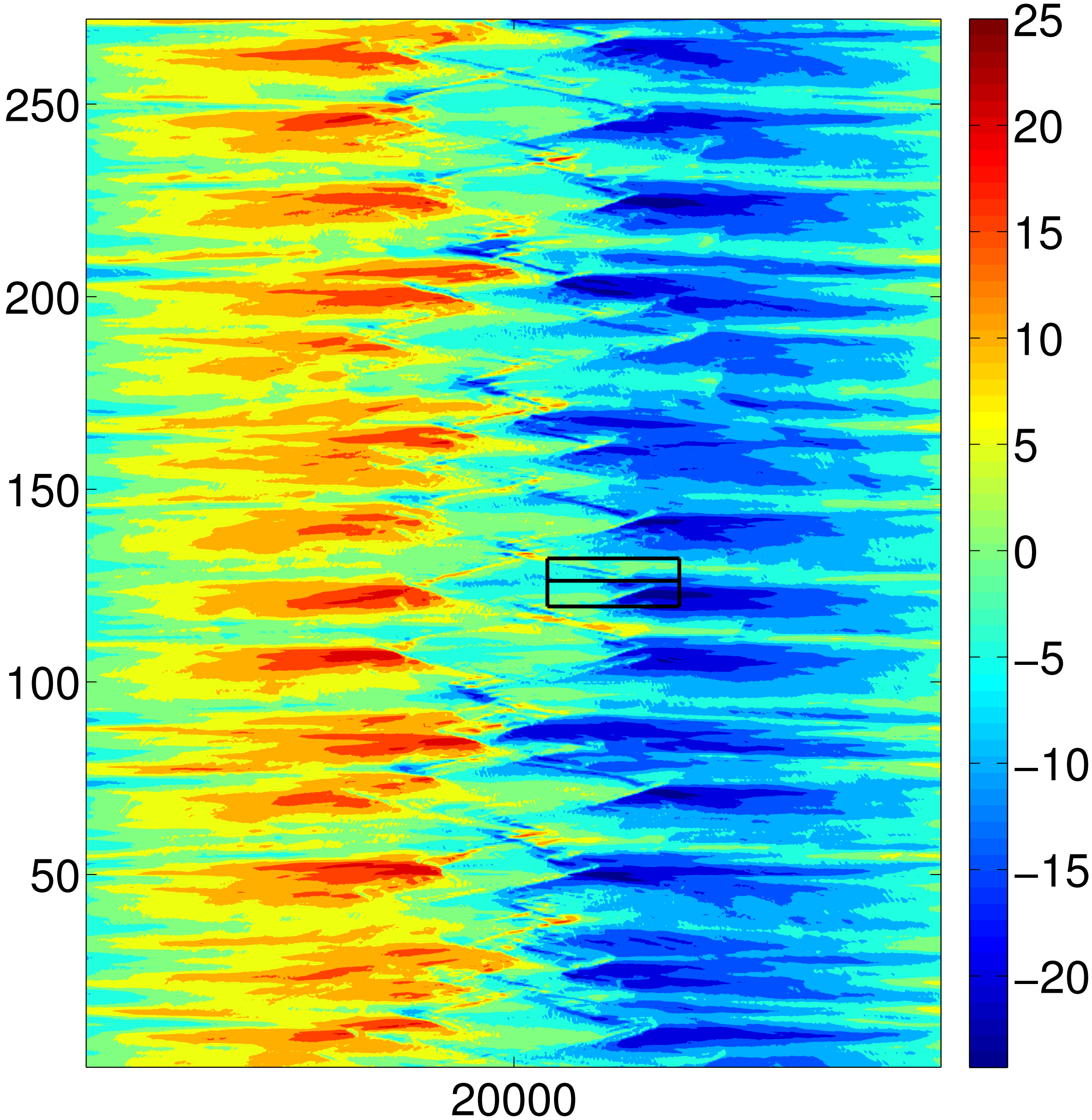

FIG. 4. Hovmoller diagram for horizontal velocity (m s^{-1}). X axis: x direction (km). Y axis: time (day).

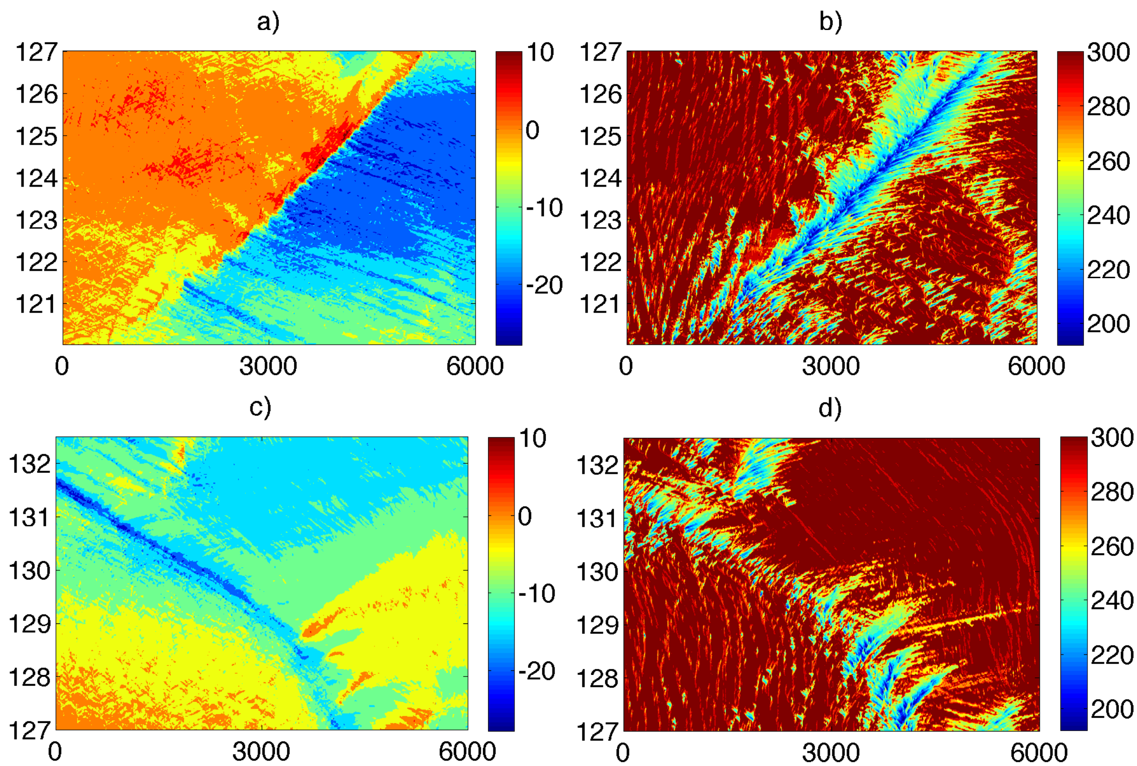

Fig. 5. Hovmoller diagram for surface wind (left column) and cloud top temperature (right column) for first (upper row) and second (bottom row) system. X axis: x direction (km). Y axis: time (day).

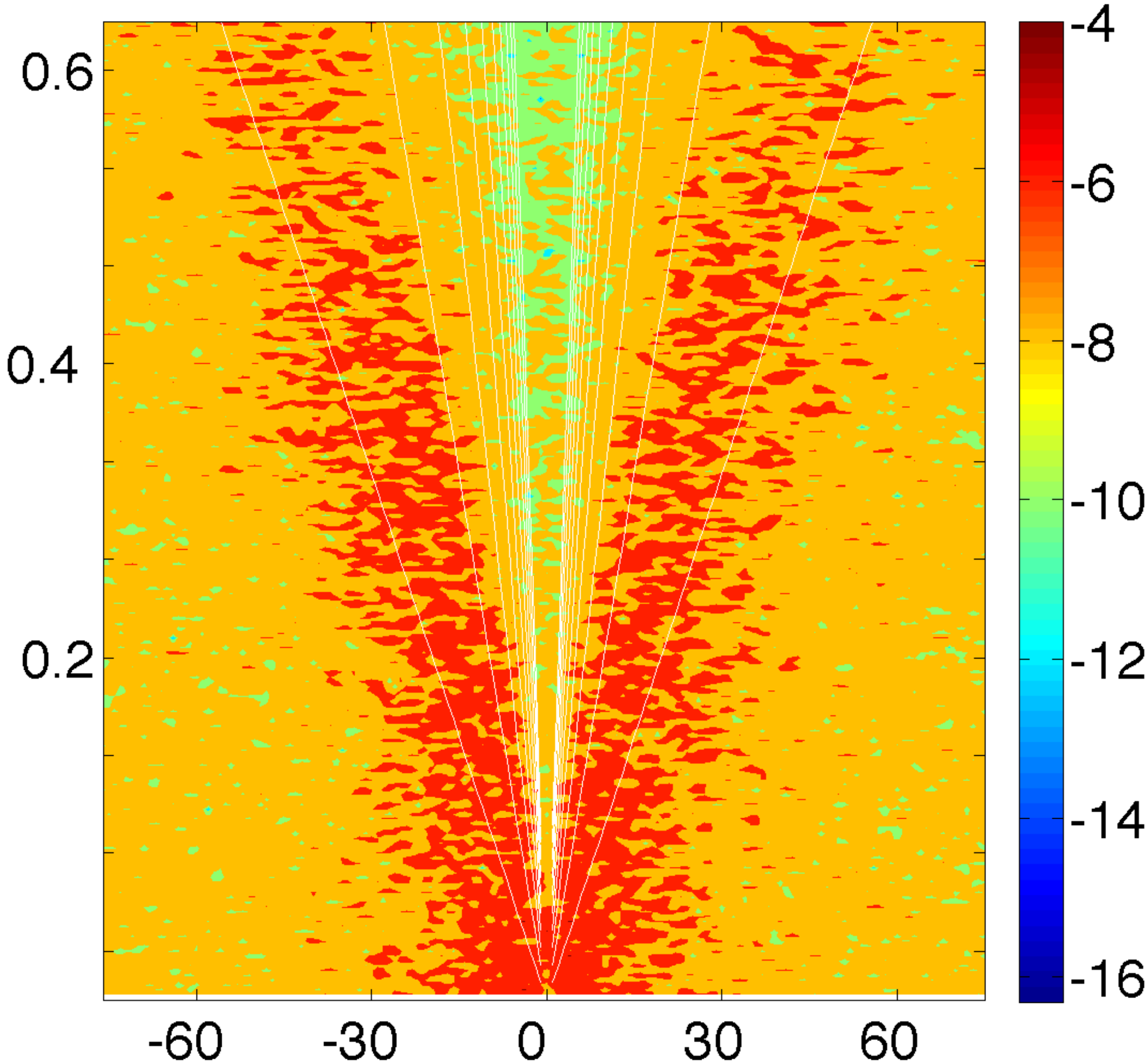

Fig. 6. Wheeler-Kiladis diagram (log(abs) of coefficients) for surface precipitation. X axis: wavenumber in space. Y axis: frequency (cycles per day). Negative/positive wavenumbers in space: westward/eastward propagation. White solid lines (from the lowest); theoretical propagation speed; every 5 m s^{-1}.

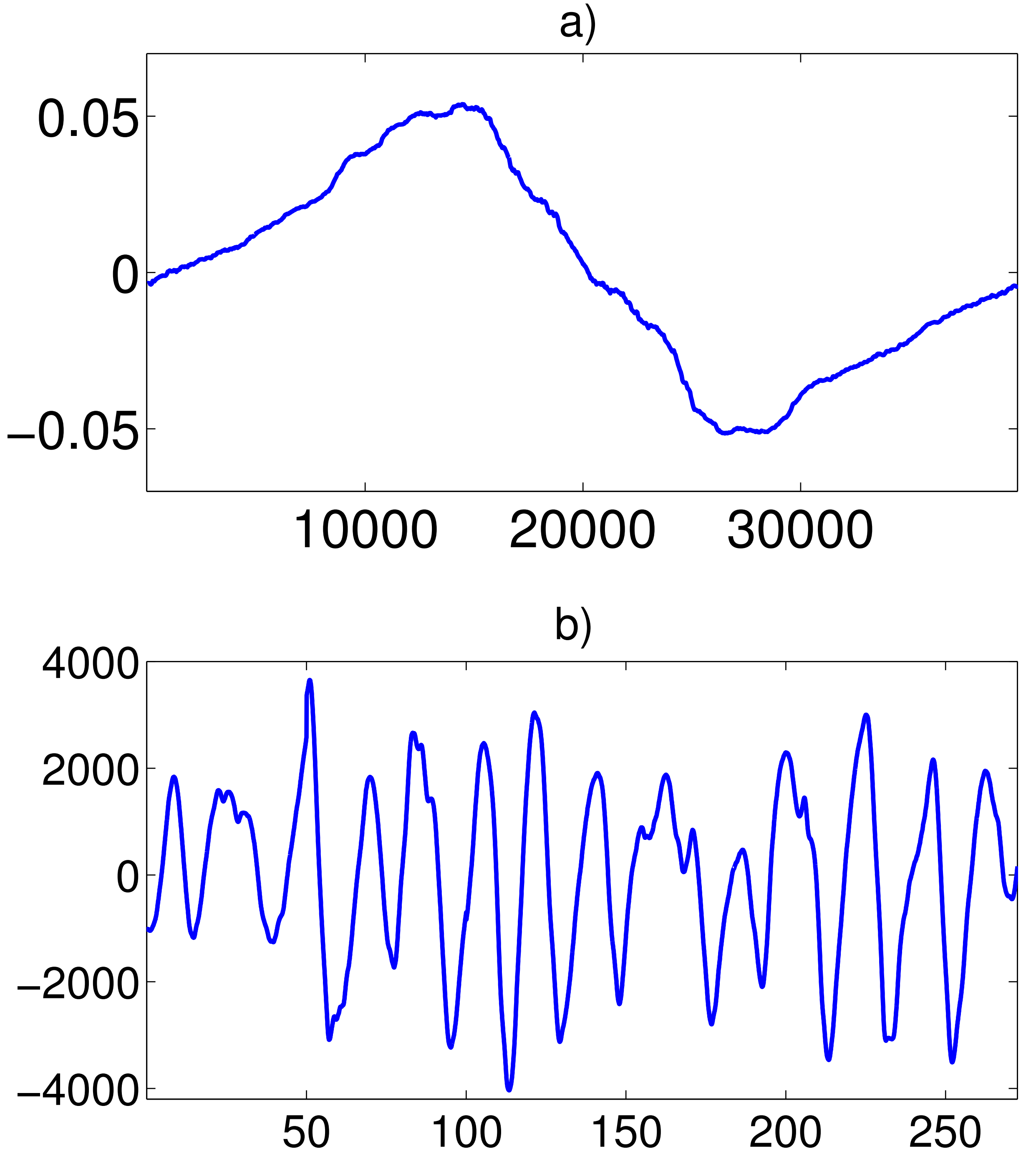

Fig. 7. Spatial pattern (a) and expansion coefficient (b) for first EOF of horizontal velocity at the first level of the model.

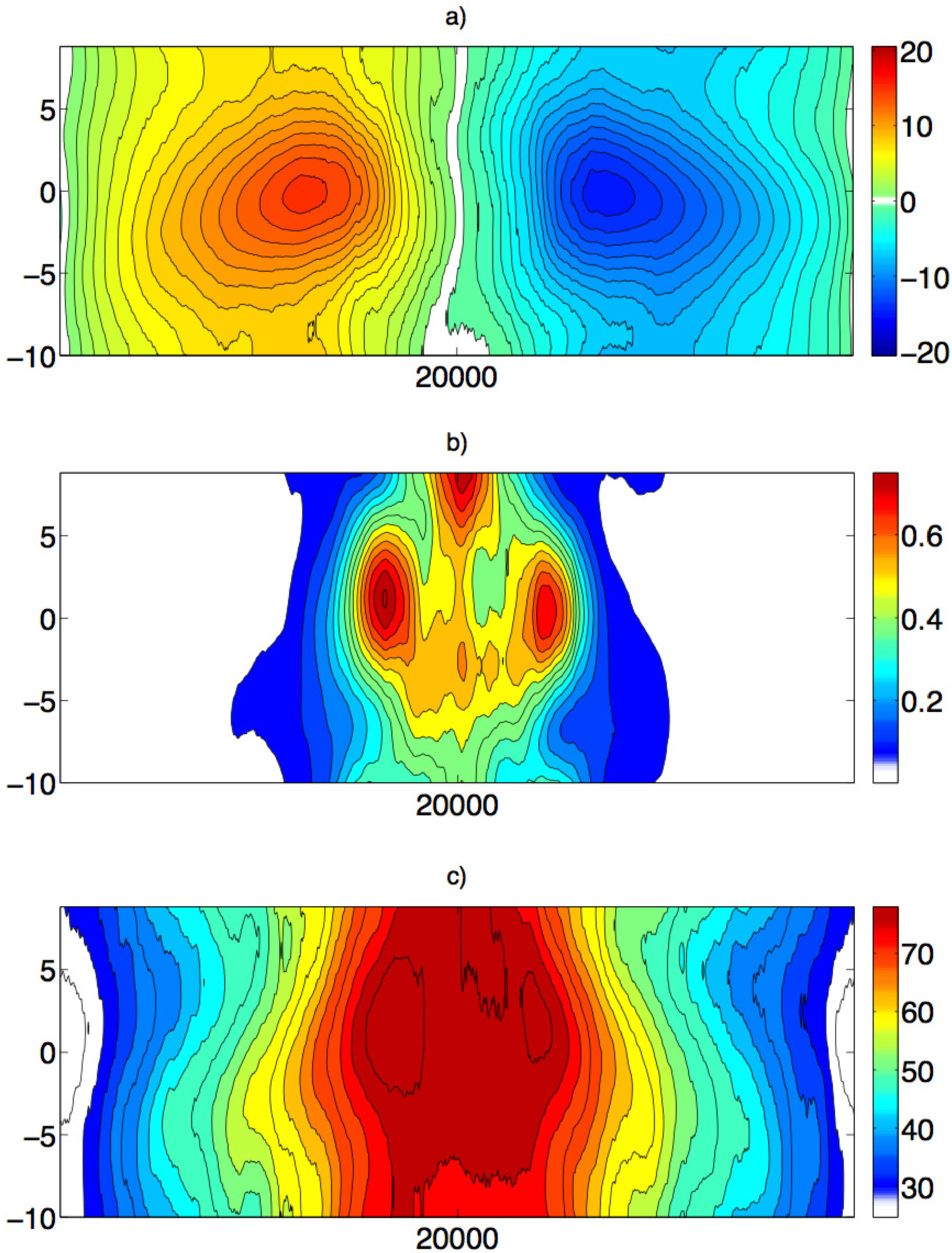

FIG. 8. Hovmoller diagram of lag regression of a) surface wind (m s^{-1}), b) precipitation (mm h^{-1}), c) precipitable water content (kg m^{-2}). X axis: x direction (km). Y axis: time (days).

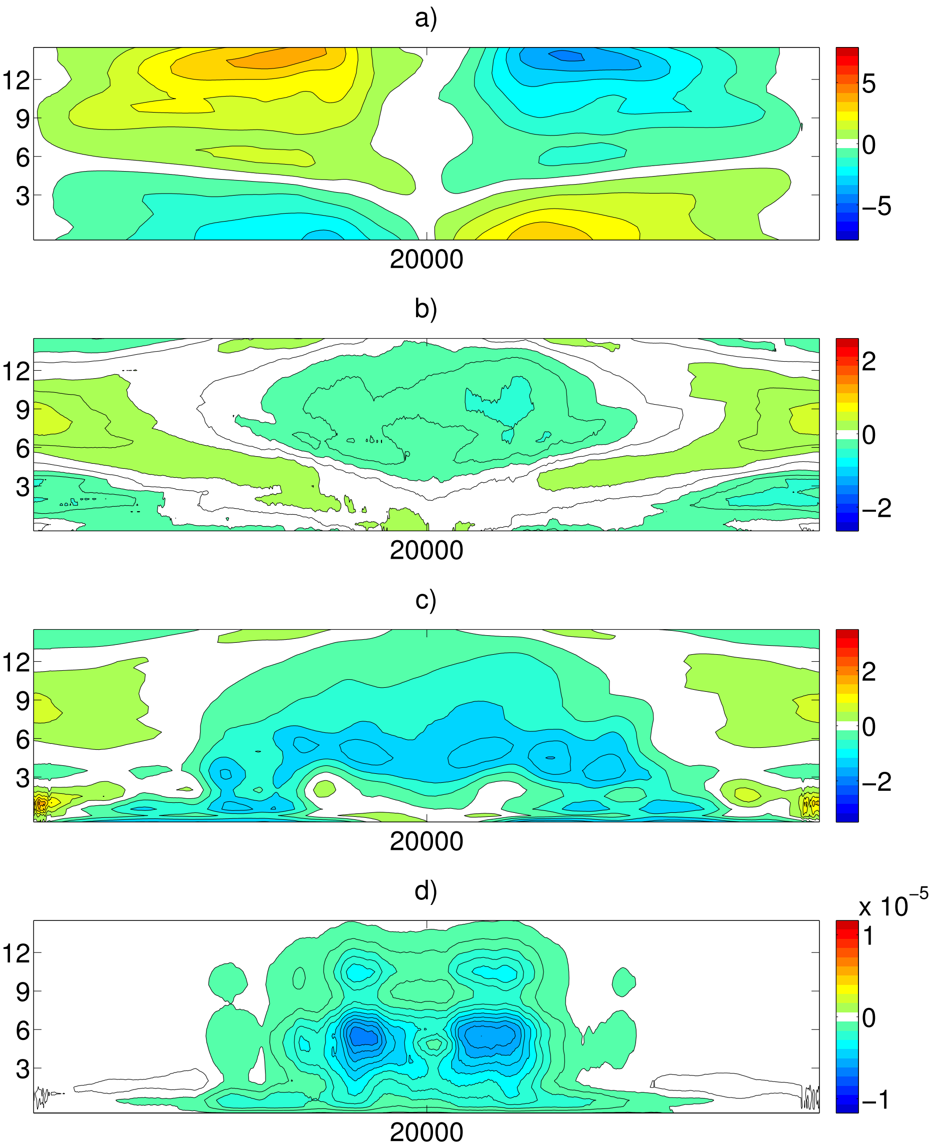

FIG. 9. Lag regressed structure during the suppressed phase for anomalies of a) horizontal velocity anomaly (m s^{-1}), b) virtual temperature (K), c) equivalent potential temperature (K), d) cloud water mixing ratio (kg kg^{-1}), for lag value of -10 day. X axis: x direction (km). Y axis: height (km).

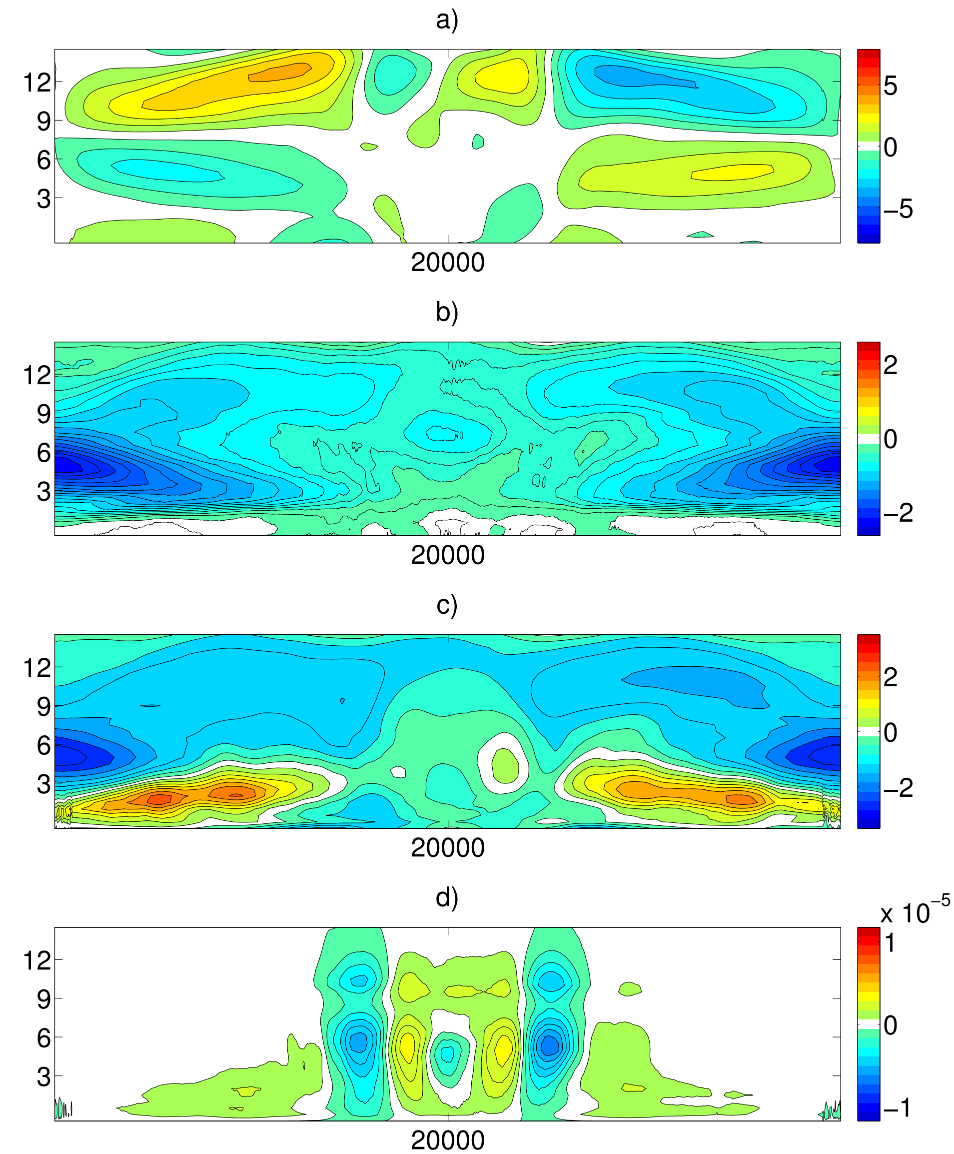

FIG. 10. Lag regressed structure during the strengthening phase for anomalies of a) horizontal velocity anomaly ($\mathrm{m\,s^{-1}}$), b) virtual temperature (K), c) equivalent potential temperature (K), d) cloud water mixing ratio ($\mathrm{kg\,kg^{-1}}$) for lag value of -5 day. X axis: x direction (km). Y axis: height (km).

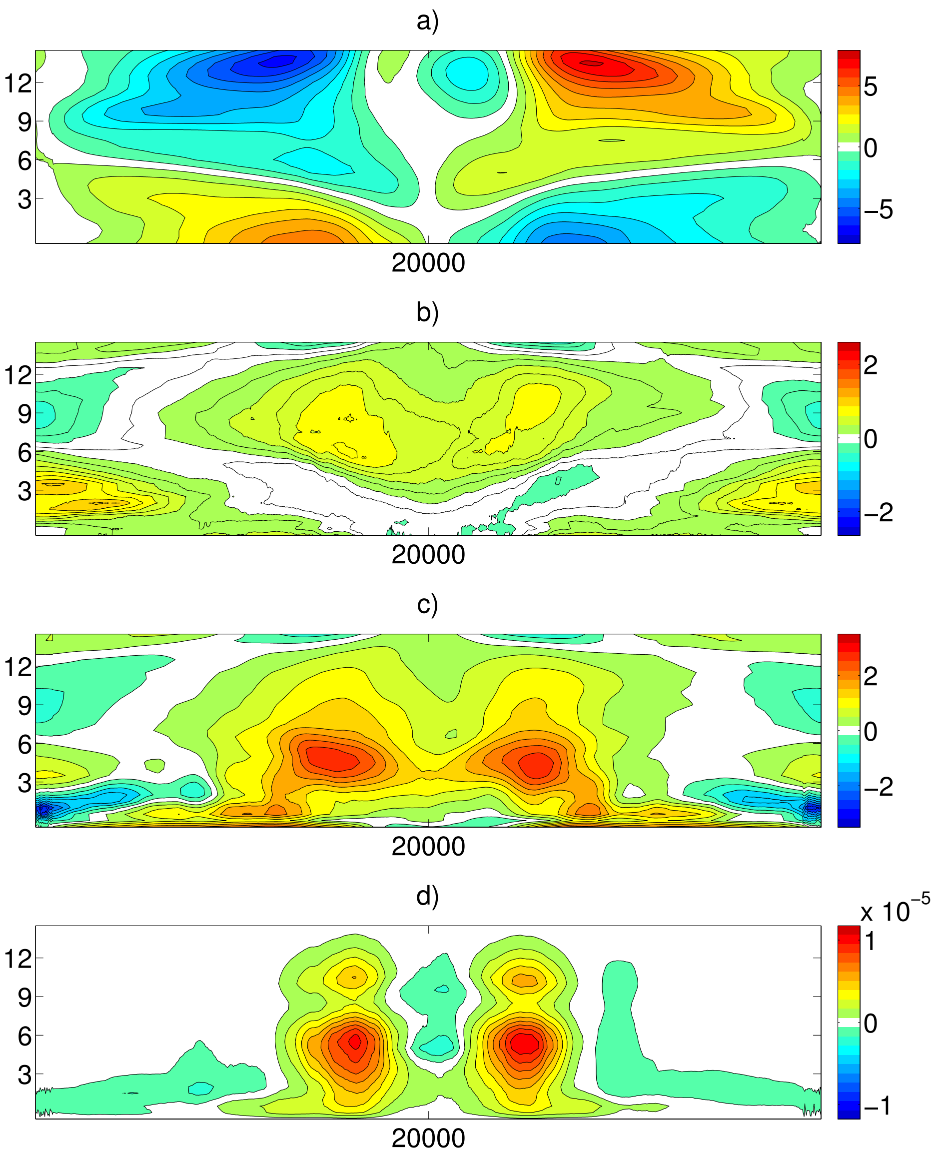

FIG. 11. Lag regressed structure during the active phase for anomalies of a) horizontal velocity anomaly (m s^{-1}), b) virtual temperature (K), c) equivalent potential temperature (K), d) cloud water mixing ratio (kg kg^{-1}) for lag value of 0 day. X axis: x direction (km). Y axis: height (km).

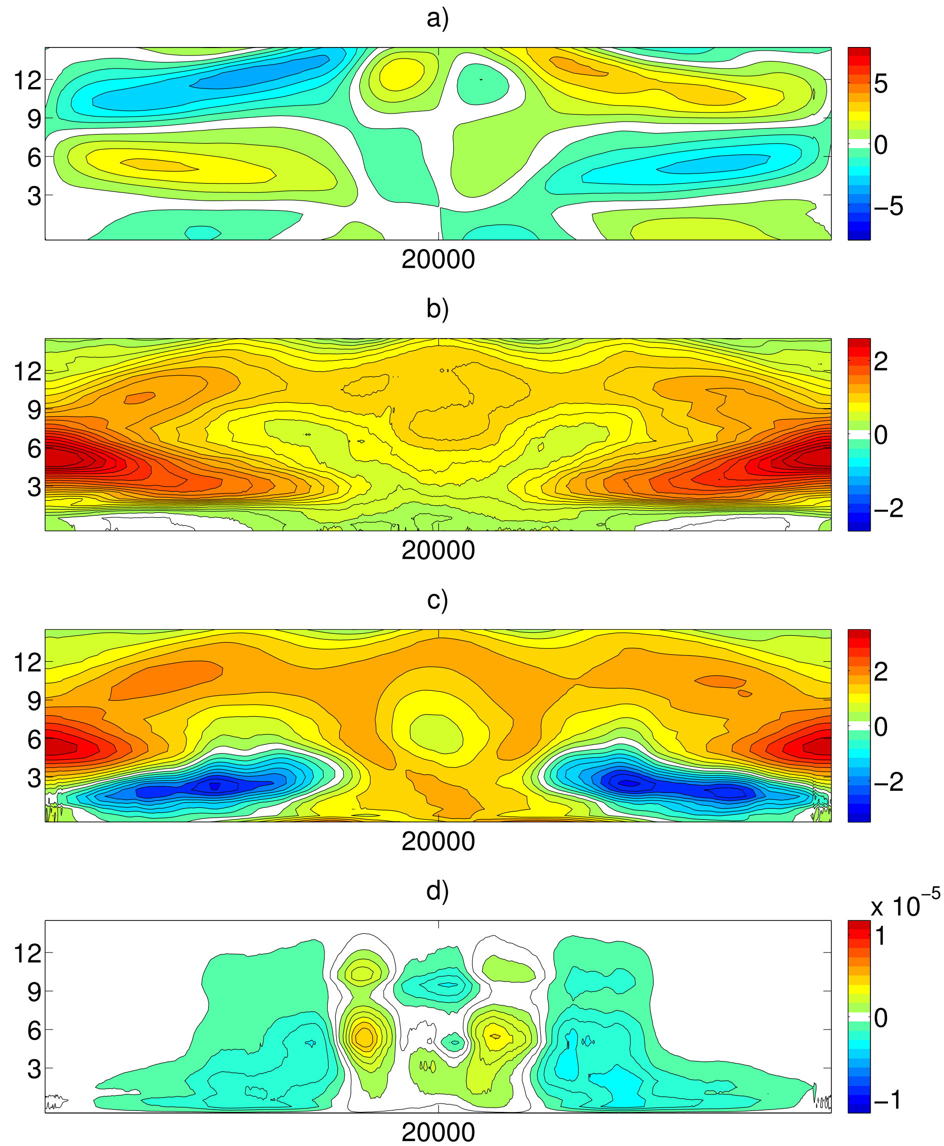

FIG. 12. Lag regressed structure during the decaying phase for anomalies of a) horizontal velocity anomaly (m s^{-1}), b) virtual temperature (K), c) equivalent potential temperature (K), d) cloud water mixing ratio (kg kg^{-1}) for lag value of 5 day. X axis: x direction (km). Y axis: height (km).

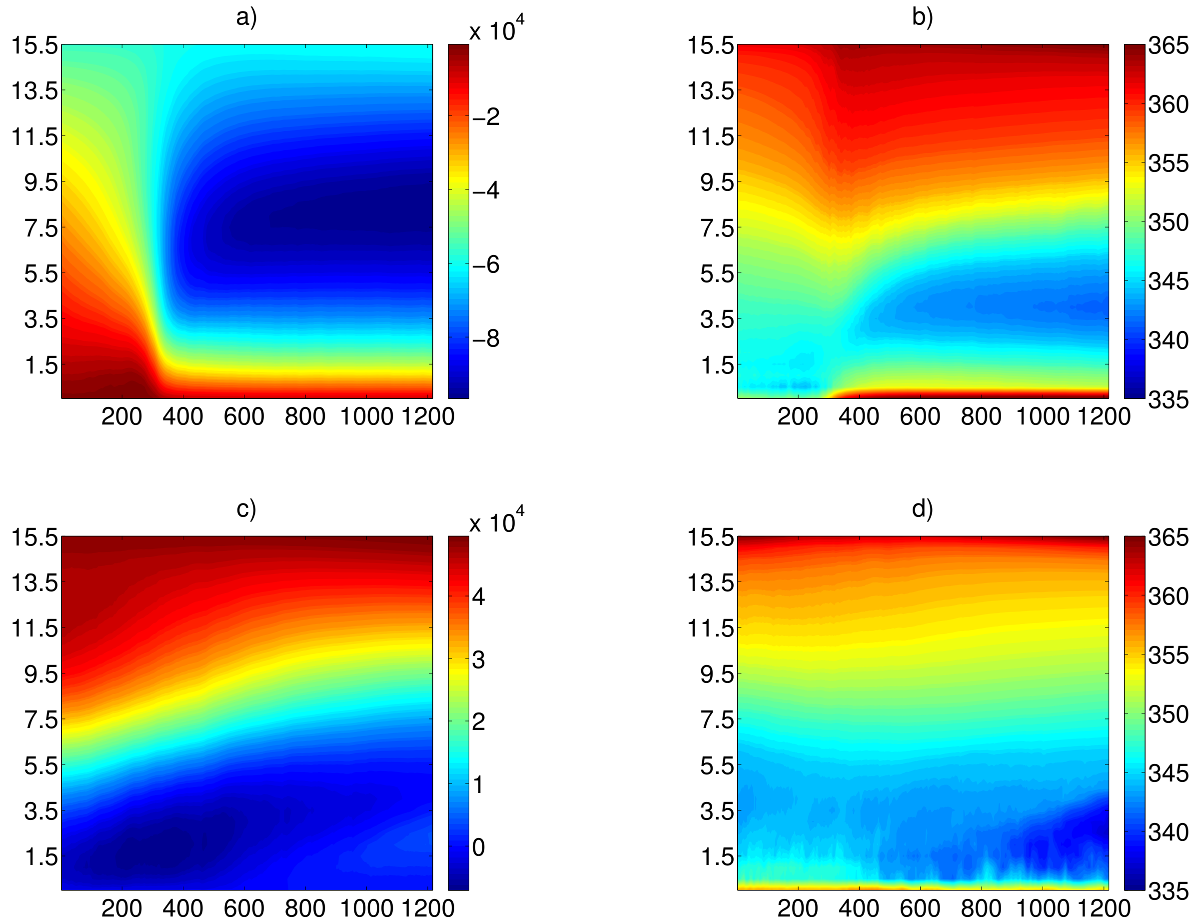

FIG. 13. Time-averaged streamfunction (left column) and equivalent potential temperature (right column) for system 1 (upper row) and system 2 (bottom row). Y axis: height (km). X axis: x direction (km)

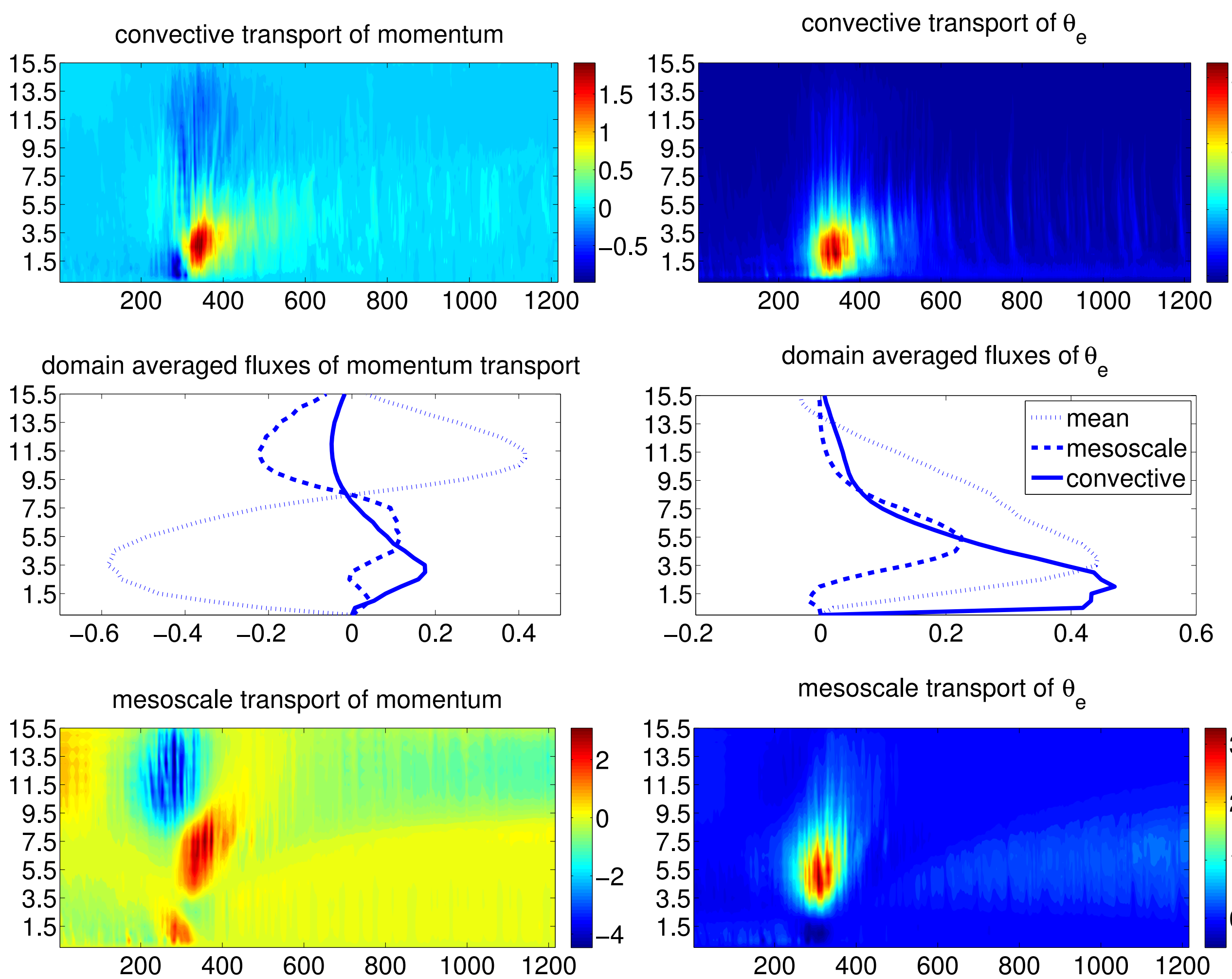

FIG. 14. Time-averaged fluxes of momentum (left) and equivalent potential temperature (right column) for system 1. Y axis: height (km). Middle row: Averaged in time and space profiles of convective (solid line) and mesoscale (dashed) fluxes, as well as fluxes associated with mean ascent(dotted line). Upper and bottom row: time-averaged spatial distribution of convective and mesoscale fluxes, respectively, over 1200 km horizontally.

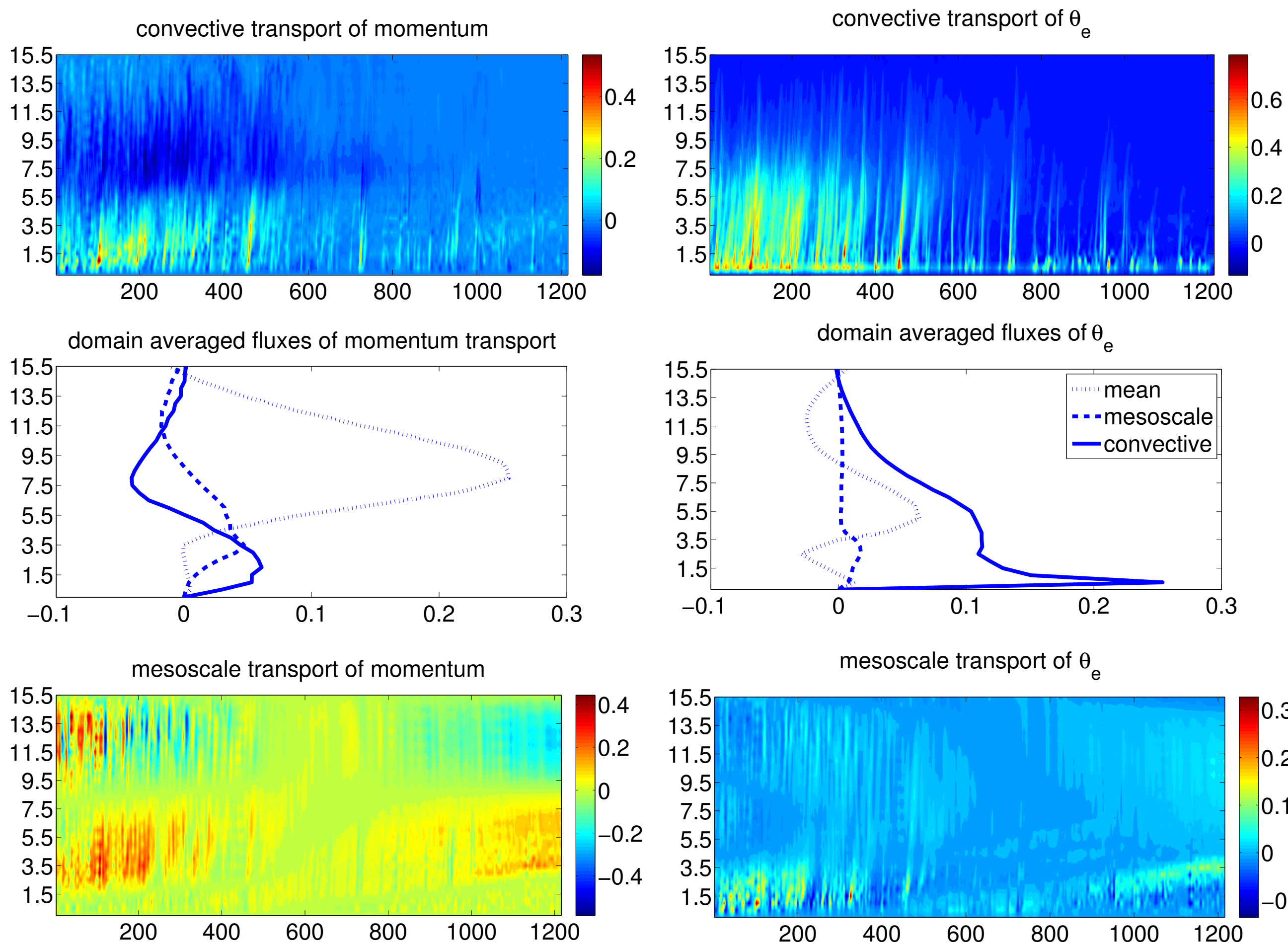

FIG. 15. Time-averaged fluxes of momentum (left column) and equivalent potential temperature (right column) for system 2. Y axis: height (km). Middle row: Averaged in time and space profiles of convective (solid line) and mesoscale (dashed) fluxes , as well as fluxes associated with mean ascent (dotted line). Upper and bottom row: time-averaged spatial distribution of convective and mesoscale fluxes, respectively, over 1200 km horizontally.